

Wake and acoustic responses of a circular cylinder to freestream fluctuations

Ronny Widjaja (1) , Andrew Ooi (1) , Li Chen (2) and Richard Manasseh (3)

(1) Department of Mechanical Engineering, University of Melbourne, Parkville, 3010, Australia

(2) Maritime Platforms Division, Defence Science Technology Organisation, Fishermans Bend, 3207, Australia

(3) Manufacturing & Infrastructure Tech., Commonwealth Scientific and Industrial Research Organisation, Highett, 3190, Australia

ABSTRACT

An upstream turbulence/fluctuation has been shown to increase the unsteadiness in the wake of a three-dimensional bluff body (Mittal, 2000). This inevitably will influence the radiated acoustic waves in the far field. In this paper, the effects of fluctuating freestream disturbances on the wake structure and sound radiation from a two-dimensional flow over a circular cylinder are investigated. The flow field is obtained by numerically solving the incompressible Navier-Stokes equations. At a Reynolds number of 40, the addition of fluctuating disturbances in the freestream causes the otherwise steady wake to oscillate at the frequency of the disturbance. This oscillation is enhanced with increasing energy and frequency of the fluctuations. The corresponding acoustic field is obtained by using an Expansion about Incompressible Flow (EIF) method. The computed acoustic field shows a dipole directivity, which is similar to that of a natural vortex shedding. Moreover, using the rms plot of the fluctuations of the EIF source terms, the location of the dipole source in the wake of the cylinder is accurately identified.

INTRODUCTION

With the increased speed of transport vehicles in recent years, vehicle noise has become one of the major environmental problems. The noise produced by commercial aircraft during take-off and landing is a concern to the community living in the vicinity of an airport. Wind noise in a car causes some discomfort to the passengers at speeds above 120 km/hr (Larsson, 2002). In order to reduce noise, many studies have been conducted to understand the mechanism of sound generation by a fluid flow. In the case of the flow over a bluff body, the vortex shedding behind the bluff body was identified as the primary drive in the sound generation process.

Recently, the study of the flow over a bluff body was extended by Mittal (2000) and Bagchi and Balachandar (2004) to include freestream turbulence. Mittal used a sinusoidally oscillating transverse velocity to represent the freestream turbulence while Bagchi and Balachandar employed a precomputed isotropic turbulent field. Despite these differences, they came up with the same conclusion that the unsteadiness in the wake region was significantly increased by the addition of the freestream turbulence. As reported by Mittal, the fluctuation of kinetic energy in the wake could reach as high as 38.6 times that in the freestream. Since the sound generation process is closely related to the wake activity, the freestream turbulence will inevitably influence the radiated sound in the far field.

In this paper, the effects of fluctuating freestream disturbances on the wake structure and sound radiation from a two-dimensional flow over a circular cylinder are investigated. The Reynolds number based on the mean flow is chosen to be 40. This corresponds to a steady wake regime with no sound radiation in the absence of the freestream disturbances. Therefore, any wake oscillation and sound radiation observed in this study are purely associated with the freestream disturbances. The effects of different forcing frequencies and intensities of the disturbances are also investigated.

SIMULATION TECHNIQUE

In the flow computation, the flow field is obtained by solving the unsteady, incompressible Navier-Stokes equations,

$$\nabla \cdot \mathbf{u} = 0, \tag{1}$$

$$\frac{\partial \mathbf{u}}{\partial t} + (\mathbf{u} \cdot \nabla) \mathbf{u} = -\nabla p + \frac{1}{\text{Re}} \nabla^2 \mathbf{u}, \tag{2}$$

where \mathbf{u} and p are the incompressible velocity vector and pressure, and Re is the Reynolds number of the flow. Without any loss of generality, an elliptic coordinate system (ξ, η) is used to express the spatial operators.

The computational domain is discretized by using a hybrid Fourier-Chebyshev collocation method. The Fourier collocation method is naturally used in the periodic azimuthal (η) direction. The collocation points are placed uniformly within $[0, 2\pi]$ with a grid spacing of $\Delta\eta = 2\pi/N_\eta$ where N_η is the number of grid points in the azimuthal direction. The Chebyshev collocation method is applied in the radial (ξ) direction. The collocation points are defined according to the following mapped Gauss-Lobatto grid distribution,

$$\xi_i = \frac{1}{2} \cos \left[\pi \left(\frac{i-1}{N_\xi-1} \right) \right] (\xi_o - \xi_n) + \frac{1}{2} (\xi_o + \xi_n), \tag{3}$$

where $i = 1, 2, \dots, N_\xi$ and N_ξ is the number of grid points in the radial direction. The terms ξ_o and ξ_n in Eq. (3) are the ξ coordinates of the cylinder and the computational boundary respectively.

In the temporal discretization, a time-split method of Streett and Hussaini (1991) is used to advance the flow field in time. A semi-implicit method is employed in order to avoid the severe numerical instabilities associated with the viscous stability limit and the pure advection limit. The viscous terms are discretized using a Crank - Nicholson method and the

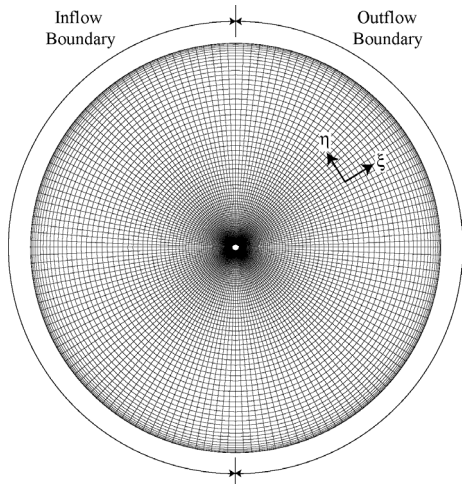


Figure 1. A typical mesh of the flow domain.

nonlinear and cross derivative terms are discretized using a third order Adams-Bashforth method.

The fluctuating freestream disturbance is introduced at the inflow boundary (see Fig. 1). It is modelled by using Mittal's sinusoidally fluctuating transverse velocity. The expression is given by

$$u_y = A_{in} \sin(2\pi\Omega t), \quad (4)$$

where A_{in} and Ω are the amplitude and nondimensional frequency of the disturbance respectively. The amplitude of the disturbance A_{in} is related to the fluctuation kinetic energy level \bar{k}_0 by $A_{in} = 2\sqrt{\bar{k}_0}$. Since viscosity will cause this disturbance to decay before reaching the cylinder, this fluctuation kinetic energy level is specified at a certain location upstream of the cylinder (l/d) where d is the cylinder's diameter, and the amplitude at the inflow boundary is then calculated accordingly. The amount of amplification can be obtained from the one dimensional convection-diffusion equation as

$$\frac{A_{in}}{A_{l/d}} = \left(\frac{\bar{k}_0}{\bar{k}_{l/d}} \right)^{\frac{1}{2}} = \exp \left[4\pi^2 \Omega^2 \left(\frac{R-l}{dRe} \right) \right], \quad (5)$$

where $A_{l/d}$ and $\bar{k}_{l/d}$ are the amplitude of the disturbance and the fluctuation kinetic energy level at the location l/d , and R is the distance between the inflow boundary and the cylinder.

In the acoustic computation, an Expansion about Incompressible Flow (EIF) method (Shen et. al., 2004) is employed to simulate the generation and propagation of the acoustic waves. It is classified as a hybrid method where the acoustic field is computed from the unsteadiness in the incompressible flow field. The governing equations for the EIF method are given by

$$\frac{\partial \rho'}{\partial t} + \frac{\partial f_i}{\partial x_i} = 0, \quad (6)$$

$$\frac{\partial f_i}{\partial t} + \frac{\partial}{\partial x_j} \left[f_i (u_{oj} + u'_j) + \rho_0 u_{oi} u'_j \right] + \frac{\partial p'}{\partial x_i} = \frac{\partial \tau'_{ij}}{\partial x_j}, \quad (7)$$

$$\frac{\partial p'}{\partial t} - c^2 \frac{\partial \rho'}{\partial t} = -\frac{\partial P}{\partial t}, \quad (8)$$

where

$$f_i = (\rho_0 + \rho') u'_i + \rho' u_{oi}, \quad (9)$$

$$\tau'_{ij} = \mu \left(\frac{\partial u'_i}{\partial x_j} + \frac{\partial u'_j}{\partial x_i} - \frac{2}{3} \delta_{ij} \frac{\partial u'_k}{\partial x_k} \right). \quad (10)$$

Here, ρ_0 , u_{oi} and P are the incompressible flow quantities, and ρ' , u'_i and p' are the acoustic quantities. Together they represent the compressible flow quantities

$$\rho = \rho_0 + \rho', \quad u_i = u_{oi} + u'_i \quad \text{and} \quad p = P + p'. \quad (11)$$

The speed of sound c in Eq. (8) is defined as $c^2 = \gamma(P + p')(\rho_0 + \rho')$ where γ is the ratio of specific heats. It is nonuniform in the acoustic field and accounts for the refraction of acoustic waves during the propagation process. The convection and nonlinear effects of the acoustic waves are also evident from Eq. (9). Moreover, the generation of the acoustic waves in this EIF method is performed through the acoustic source term on the right hand side of Eq. (8). This acoustic source term depends on the unsteadiness of the pressure field, which is very similar to the dilatation theory in Ribner's acoustic analogy (Ribner, 1959).

To compute the acoustic field, the spatial and temporal operators in Eq. (6) – (8) are discretized by using an eleven-stencil-points Dispersion-Relation-Preserving (DRP) method (Bogey and Bailly, 2002) and a fourth order Runge-Kutta method respectively. The DRP method is an optimised finite difference method with a better wave resolution property than a simple finite difference method. It only requires 4.65 points per wavelength to resolve the acoustic waves as compared to 6.58 points per wavelength for a finite difference method of the same stencil size. The superior wave resolution is evident from the group velocity plot in Fig. 2. The group velocity of the finite difference method is observed to deviate earlier from unity, resulting in a larger dispersion error.

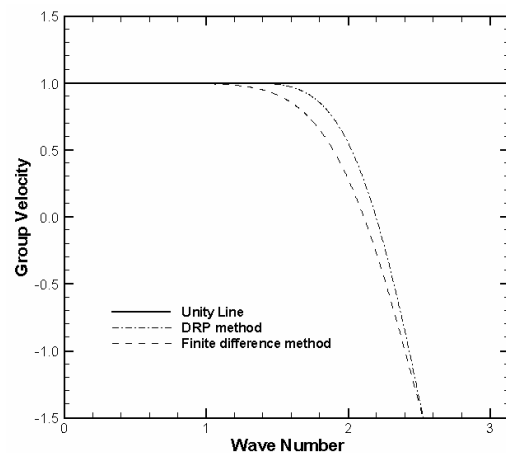


Figure 2. Group velocities of the eleven-stencil-points DRP method and the finite difference method.

At the computational boundary, a Perfectly-Matched-Layer (PML) absorbing boundary condition (Hu, 2001) is applied. The acoustic waves are smoothly attenuated in this absorbing layer before reaching the computational boundary. Twenty radial grid points are allocated for this absorbing layer to ensure a perfectly nonreflecting condition is achieved.

Due to the larger acoustic wavelength, the acoustic domain extends beyond the flow domain. A hyperbolic tangent mapping function is used in the radial direction to achieve appropriate grid spacings in both near and far fields. The grid

stretching in this mapping function is limited to $lsf_{max} = 0.05$ in order to avoid any generation of spurious waves. Here, $lsf = \frac{r_{i+2} - r_{i+1}}{r_{i+1} - r_i} - 1$ is the local stretching factor in the grids and r_i is the radial location of the grid point i . On the other hand, the grid spacing in the azimuthal direction is kept constant. The value is the same as that in the flow domain.

RESULTS

In the current study, three different configurations of the freestream disturbances are considered. They are listed in Table 1. The fluctuation kinetic energy level $\bar{k}_{1/d}$ in the table corresponds to an upstream location $l/d = 5$. The intensities of the fluctuations I are also provided in the fourth column. It is defined as the ratio between the root-mean-squared (rms) value of the freestream fluctuations to the freestream streamwise velocity, $I = v_{rms} / u_{\infty}$, where $v_{rms} = A_{1/d} / \sqrt{2}$. The maximum value of v_{rms} investigated here is 10% of the mean flow velocity.

The flow and acoustic domains used in the computations remain the same for all cases. The former has a radius of $30d$ and is discretized by using 100×160 grid points in the radial and azimuthal directions respectively. The acoustic domain extends to $220d$ including the PML absorbing layer. It comprises of 400×160 grid points with radial grid spacings of 0.05 in the near field and 2 in the far field.

Table 1. Parametric range of the freestream disturbances.

Case	$\bar{k}_{1/d}$	Ω	I
1	0.002	0.06	6.3%
2	0.002	0.1	6.3%
3	0.005	0.1	10%

Flow Field

Consistent with classical experimental and numerical results, data from the incompressible flow calculation (without any freestream disturbance) shows a steady wake behind the cylinder if there are no disturbances upstream. A pair of recirculation bubbles is observed in the wake (see Fig. 3a). They are $2.26d$ in length, measured from the downstream surface of the cylinders. The separation points were found to be $\pm 53.7^\circ$ from the positive x direction. These results agree well with earlier data presented in Coutanceau and Bouard (1979) and Dennis and Chang (1970). Despite the relatively short length of the recirculation bubbles, the shear layers in the steady wake extend to a considerable distance downstream. This is evident from the steady state vorticity field in Fig 3b.

Upon adding the freestream disturbances, the wake behind the cylinder becomes unsteady which is obvious from the instantaneous vorticity plots shown in Fig. 4. They are taken at the time instant when a maximum lift occurs. The responses of the wake are shown to depend on the nature of the freestream disturbances. For a low frequency disturbance $\Omega = 0.06$ (case 1), the shear layers are observed to oscillate in the transverse direction at the disturbance frequency. The wake appears to have enough time to respond to the disturbance so that no significant interaction between the two shear layers is observed. As a result, the shear layers remain

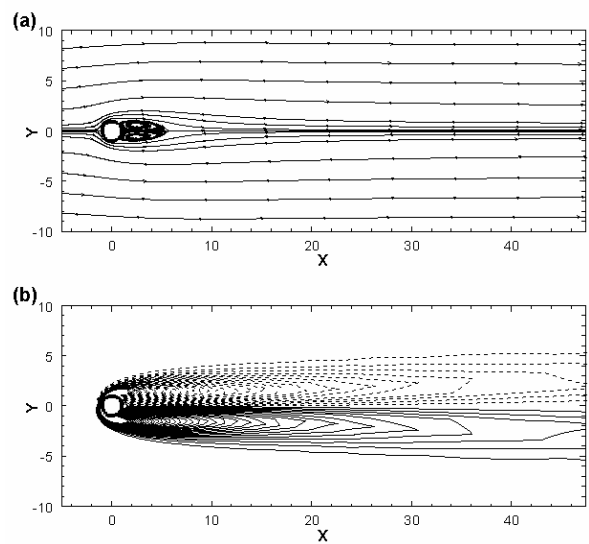


Figure 3. Plots of (a) streamlines and (b) vorticity field. Solid and dashed lines represent positive and negative contour levels respectively. Contour levels are from -0.2 to 0.2 with an increment of 0.025.

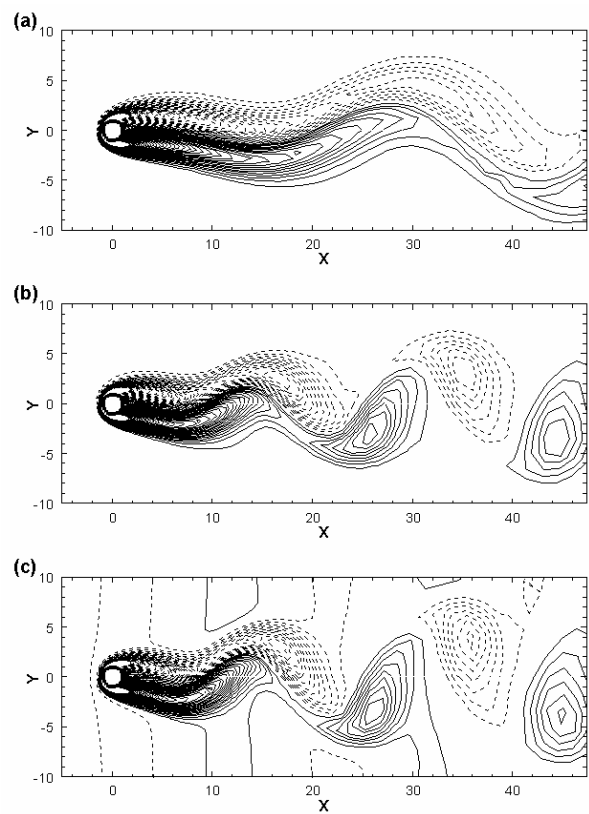


Figure 4. Vorticity fields of (a) case 1, (b) case 2 and (c) case 3. Solid and dashed lines represent positive and negative contour levels respectively. Contour levels are from -0.2 to 0.2 with an increment of 0.025.

integrated structures in spite of the oscillations. This phenomenon was also observed by Mittal (2000) in the flow over a sphere at $Re=150$ with a low frequency freestream disturbance.

For a higher frequency of freestream fluctuation $\Omega = 0.1$ (case 2), the freestream disturbance causes the shear layers to interact. They become unstable at a certain distance in the wake and this results in the formation of discrete vortices.

This vortex formation is similar to the vortex shedding process where positive and negative vortices are produced in

turn, one after the other. The frequency of this vortex formation is the same as the disturbance frequency.

Increasing the fluctuation kinetic energy level in the upstream to $\bar{k}_{1/d} = 0.005$ (case 3) only moves the instability point in the upstream direction. The vortex formation process remains the same. However, Fig. 4c features transverse contour levels that are not seen in the earlier cases. These transverse contour levels correspond to the vorticity sheets produced by sinusoidally oscillating the transverse velocity in the upstream. Their magnitudes are large enough to be observable within the given contour levels. The regions between two transverse solid lines contain the local peak positive vorticity of the disturbance while the regions between two transverse dashed lines contains the local peak negative vorticity of the disturbance.

On the other hand, the local peak positive and negative transverse velocities of the disturbance occur in between the transverse solid and dashed lines. The former is located downstream of the solid lines while the latter is located downstream of the dashed lines. By using this information, the negative vortex is observed to form when the maximum transverse velocity pushes the positive vorticity shear layer upward and disintegrates a fraction of the shear layer with negative vorticity. The reverse is also true for the formation of a positive vortex.

Furthermore, it is commonly found in multiphase particulate flows that the interaction between the freestream disturbance and the particulates can result in either an increase or a decrease in the fluctuations of kinetic energy in the flow. Gore and Crowe (1989) showed that this disturbance enhancement and suppression depended only on the ratio between the particulate size d_p and the characteristic length of the disturbance l_e . The critical ratio was given by $d_p/l_e = 0.1$, above which the freestream disturbance were enhanced. Hestroni (1989) on the other hand demonstrated that the enhancement and suppression processes depended on a few parameters, which collectively formed the particulate Reynolds number

$$Re_p = \frac{(u_f - u_p)d_p(\rho_p - \rho_f)}{\mu_f}, \quad (11)$$

where u_p and ρ_p correspond to the velocity and density of the particulate, and u_f , ρ_f and μ_f correspond to velocity, density and dynamic viscosity of the flow medium.

For the interaction between the freestream disturbance and a single particulate, which was modelled as a sphere, Mittal (2000) and Bagchi and Balachandar (2004) reported disturbance enhancements in almost all of their simulations. Only one case of disturbance suppression was reported by Bagchi and Balachandar, which occurred at a high disturbance intensity and with an intermediate sphere size.

Following Mittal, the fluctuation kinetic energy level \bar{k} at every point in the flow field is computed and normalized by the upstream fluctuation kinetic energy level $\bar{k}_{1/d}$. The expression is given by

$$\frac{\bar{k}}{\bar{k}_{1/d}} = \frac{\frac{1}{2} \left[\overline{(u - \bar{u})^2} + \overline{(v - \bar{v})^2} \right]}{\bar{k}_{1/d}}, \quad (12)$$

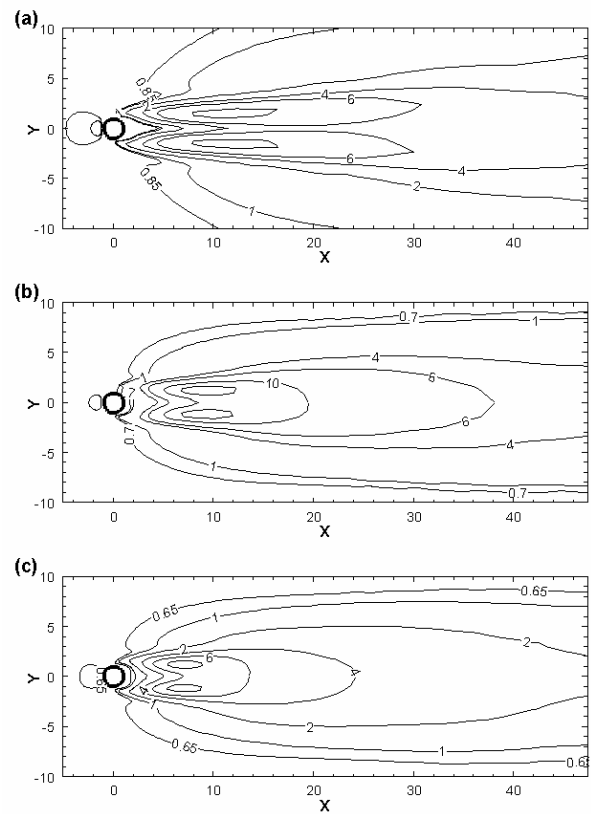


Figure 5. Fluctuation kinetic energy fields of (a) case 1, (b) case 2 and (c) case 3.

where the overbar represents time averaged quantities. This ratio determines the amount of enhancement or suppression of the freestream disturbances. Disturbance enhancement is characterised by $\bar{k}/\bar{k}_{1/d} > 1$ while disturbance suppression is characterised by $\bar{k}/\bar{k}_{1/d} < 1$.

Figure 5 shows the normalized fluctuation kinetic energy levels for the three cases listed in Table 1. The freestream disturbances are enhanced in all cases with regions of $\bar{k}/\bar{k}_{1/d} > 1$ existing in the wake of the cylinder. Two local maximum amplifications are observed in the fields. They are located at distances of $5.5d$, $4.5d$ and $3.1d$ from the cylinder surface in cases 1, 2 and 3 respectively. This location of maximum amplification is clearly shown to move upstream with an increase in the disturbance frequency and intensity. Away from the wake region, reductions in the freestream disturbances are also observed. However, these reductions are due to the dissipation effect rather than the interaction between the disturbances and the circular cylinder.

The maximum amplification factors in cases 1, 2 and 3 are 11.5, 14.3 and 8.7 respectively. These data show that the freestream disturbances are significantly enhanced in the wake of the cylinder. These amplifications remain quite strong even at a considerable distance downstream. The amplification factor is still larger than 4 for cases 1 and 2, and 2 for case 3 at the location $20d$ downstream.

Furthermore, the increase in the disturbance frequency (from case 1 to case 2) is shown to result in an increase in the amplification factor. This can be attributed to the increased activities in the shear layer that leads to the formation of discrete vortices. On the other hand, a further increase in the disturbance intensity (from case 2 to case 3) actually decreases the amplification factor. This is because the increase in the fluctuation kinetic energy in the wake is

hindered by the freestream fluctuation kinetic energy, which has a higher magnitude in case 3. As a result, the ratio of the downstream fluctuation kinetic energy to that in the upstream becomes smaller.

Apart from the flow structure and fluctuation kinetic energy level in the wake, the freestream disturbance also affects the lift and drag forces on the circular cylinder. The oscillations of these lift and drag forces are summarised in the lift-drag phase plot in Fig. 6. In the absence of the freestream disturbance, no lift is produced and the drag coefficient is computed as 1.52. With the addition of freestream disturbances in cases 1, 2 and 3, these lift and drag forces fluctuate in time. The lift fluctuation has the same frequency as the disturbance frequency while the frequency of the drag fluctuation is twice the disturbance frequency.

The mean lift force remains zero for all cases but the mean drag force increases with the increase in frequency and intensity of the disturbance. The mean drag coefficients for cases 1, 2 and 3 are 1.54, 1.58 and 1.61 respectively. The fluctuations of the lift and drag forces are also found to behave in the same manner as the mean drag coefficient. The former are given by 0.127, 0.140 and 0.231, and the latter are given by 0.00304, 0.00369, 0.00896.

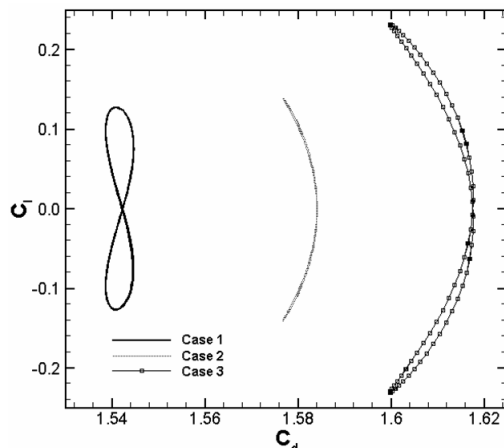


Figure 6. Lift-drag phase plots.

Acoustic Field

In the aerodynamically generated sound, the acoustic waves are produced by the unsteadiness in the flow field. This implies that the steady wake in Fig. 3 does not produce any sound radiation. Therefore, the acoustic waves produced in cases 1, 2 and 3 are purely associated with the freestream disturbances. The instantaneous acoustic fields in these cases are given in Fig. 7. The acoustic waves were clearly shown to come from the flow regions at the center of the acoustic domain. They are stronger in the transverse direction, giving a dipole characteristic to the sound radiation pattern. This dipole characteristic is also supported by the directivity plots in Fig. 8 where the curves bulge in the transverse direction. These directivity plots are obtained by computing the circumferential sound pressure level at a radius of $200d$. The expression of the sound pressure level is given by

$$SPL = 20 \log_{10} \left(\frac{p'_{rms}}{2 \times 10^{-5}} \right), \tag{13}$$

where p'_{rms} is the rms value of the acoustic pressure fluctuations.

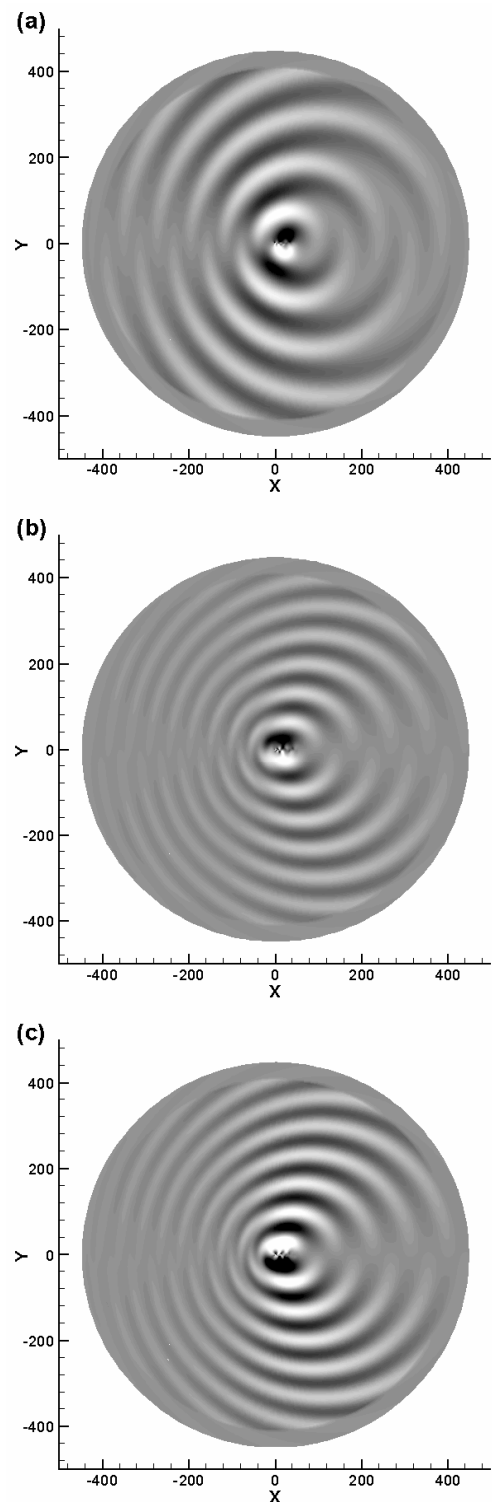


Figure 7. Acoustic pressure fluctuation fields of (a) case 1, (b) case 2 and (c) case 3. White and black contours represent the crests and troughs of the acoustic waves respectively. Their intensities are associated with the amplitudes of the waves.

As shown in Figures 7 and 8, the peak intensities of the acoustic waves occur at angles of $\pm 97^\circ$ measured from the positive x axis. The margin of error is given by $\pm 2.75^\circ$. This slight upstream directivity is similar to the acoustic radiation produced by a circular cylinder in the natural vortex shedding regime (Inoue, 2002). Inoue showed that this slight upstream directivity was due to the Doppler effect, which

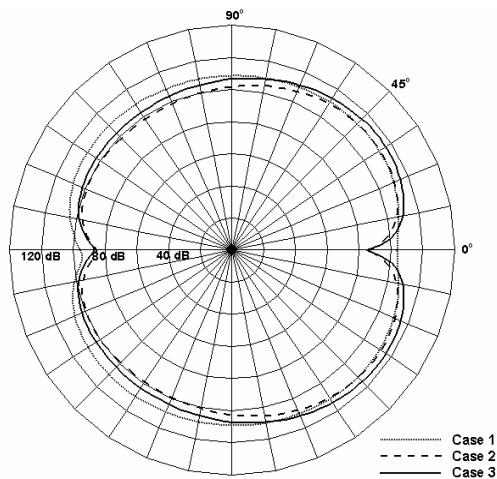


Figure 8. Directivities of acoustic waves at a radius of $200d$ from the cylinder.

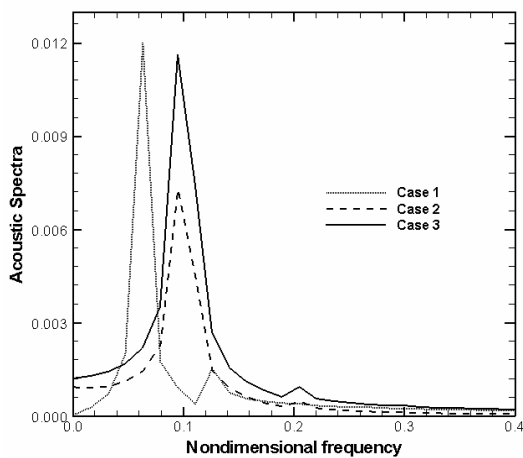


Figure 9. Acoustic spectra at an observation point located at $200d$ above the cylinder.

intensified the upstream portion of the acoustic waves. Without the Doppler effect, Inoue showed that the acoustic waves from a natural vortex shedding would have peak intensities at angles close to $\pm 90^\circ$. Moreover, Fig. 7 also shows that the acoustic waves are completely attenuated by the PML absorbing boundary condition before reaching the computational boundary. Owing to the absorbing layer, no significant acoustic waves are reflected back to the computational domain.

In contrast to the slight upstream directivity in case 1, the acoustic field produced by a higher frequency disturbance (case 2) shows peak intensities at angles of $\pm 70^\circ$. The margin of error is the same for both cases. The difference in the directivities between cases 1 and 2 can be explained by the difference in the wake structures in those cases. The wake in case 1 is slowly modulated by the freestream disturbance without any significant interaction between the shear layers while the wake in case 2 involves a vortex formation from the instability in the shear layers. The latter was also observed in the mixing layer case where the discrete vortices produced by the mixing layer instability caused a slight downstream directivity (Colonus et. al., 1997). Moreover, the higher disturbance intensity in case 3 only produces a higher sound intensity while the directivity remains the same as in case 2.

Furthermore, the wavelengths of the radiated waves appear to be shorter in the upstream than those in the downstream. This is because the effective propagation speeds of the acoustic waves are modified by the effect of mean flow convection. In

the upstream, the effective propagation speed is reduced, producing shorter wavelength waves. The reverse is true downstream of the cylinder. This is an illustration of Doppler shift owing to the mean flow.

On the other hand, the acoustic waves that propagate at angles $\pm 90^\circ$ travel at the ambient speed of sound and maintain the original wavelengths. These original wavelengths can be obtained from the acoustic spectra in Fig. 9. These spectra are computed from the temporal evolutions of the acoustic pressure fluctuations at an observation point located at $200d$ above the cylinder. They clearly show two distinct peaks at two different frequencies. The lower frequency is the dominant frequency that characterizes the frequency and wavelength of the radiated acoustic waves while the higher frequency is in fact only a harmonic of the lower one.

As expected, the dominant frequencies in cases 1, 2 and 3 are found to be close to the frequencies of the freestream disturbances. Small differences exist but they are believed to be caused by insufficient sampling rate. By using the dominant frequencies obtained from Fig. 9, the wavelengths of the radiated acoustic waves in cases 1, 2 and 3 are computed as 106, 71 and 71 respectively.

Acoustic Source Identification

In hybrid methods, the sound generation due to the flow evolution is provided by the acoustic source terms on the right hand side of the governing equations. These acoustic source terms therefore can be used to determine the exact location of the acoustic sources in the flow region. This approach was used by Iida et. al. (2004) to identify the acoustic sources in the wake of a rotating circular cylinder. They chose the acoustic source term in Powell's acoustic analogy for this purpose. Its expression is given by

$$S_{Powell} = \rho_0 \nabla \cdot (\boldsymbol{\omega} \times \mathbf{u}), \tag{14}$$

where ρ_0 is the ambient density, $\boldsymbol{\omega}$ and \mathbf{u} are the vorticity and velocity vectors respectively. This Powell's source term was chosen among others because it was compact in space and gave a direct relationship between the vorticity fluctuation and the sound generation.

In their analyses, regions of high contour levels of the acoustic sources were identified as the locations of the acoustic sources. Nevertheless, higher contour levels of acoustic sources do not necessarily produce stronger acoustic waves. This is because the acoustic waves are generated by the fluctuations in the acoustic sources. It is not due to the intensity of the acoustic sources. This point was also acknowledged by Iida et.al. (2004) who discovered that the radiated acoustic waves were weaker at a higher rotation rate despite the increasing intensity of the acoustic sources. However, no further attempt was made to give a better identification of the acoustic sources.

In this paper, an effective acoustic source term is proposed. It is based on discarding the time-averaged value of the acoustic source term. Its expression is given by

$$S_{eff} = S - \bar{S}, \tag{15}$$

where S_{eff} and \bar{S} are the effective and time-averaged acoustic source terms. The EIF acoustic source term in Eq. 8 is

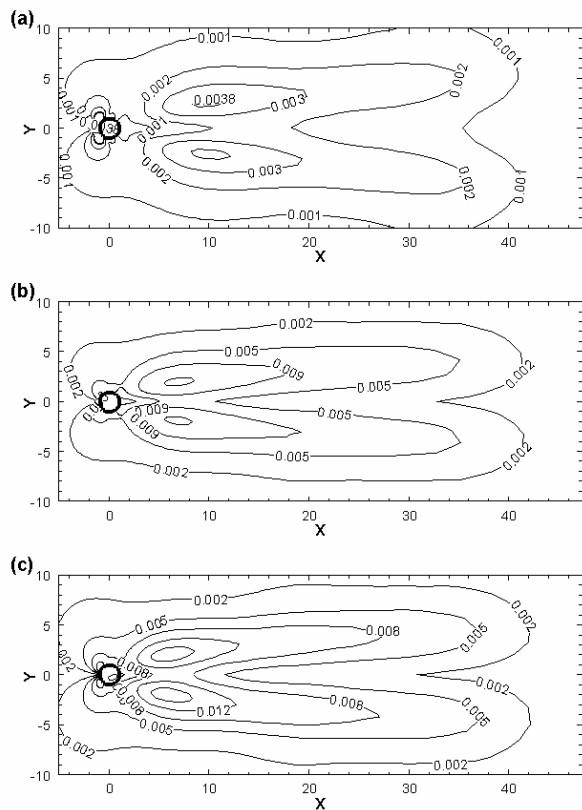


Figure 10. Acoustic source rms fields of (a) case 1, (b) case 2 and (c) case 3.

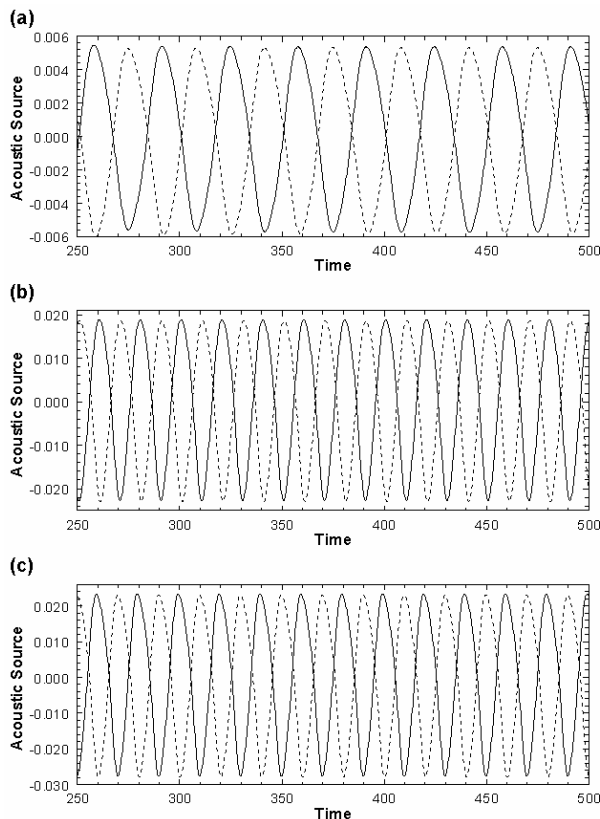


Figure 11. Time evolution of the acoustic source at the local maximas. Solid and dashed lines correspond to the top and bottom maximas respectively.

employed here to determine the location of the acoustic sources. Since this EIF acoustic source term involves a time derivative, its time average vanishes for a periodic problem $\bar{S} = 0$. Therefore,

$$S_{eff} = S = -\frac{\partial P}{\partial t}. \tag{15}$$

The rms of this acoustic source term is plotted in Fig. 10. In all cases, two local maximas can be identified behind the circular cylinder. They are located at distances of $4.7d$, $3d$ and $2.5d$ from the downstream surface of the cylinder. They are clearly shown to move upstream with the increase of disturbance frequency and intensity.

These local maximas represent the local maximum fluctuations of the acoustic sources. Since the fluctuations at the top and bottom local maximas are 180° out of phase (see Fig. 11), they form dipole type acoustic sources that produce acoustic waves in the transverse direction. In cases 2 and 3, these local maximas represent the dominant acoustic sources. In case 1 on the other hand, another pair of local maximas exists on the upstream surface of the cylinder. These local maximas also form a dipole type acoustic source. They in fact have larger fluctuations than those behind the cylinder, making them the dominant acoustic source in case 1.

CONCLUSION

In conclusion, the effects of three different configurations of freestream disturbance on the wake and acoustic radiation are investigated. The lower frequency disturbance (case 1) produces a slow oscillation in the wake and acoustic waves with peak intensities at angles of $\pm 97^\circ$. The higher frequency disturbance (case 2) on the other hand causes the shear layers to break and form discrete vortices. This results in acoustic waves with peak intensities at angles of $\pm 70^\circ$. Finally, increasing the disturbance intensity from 6.3% in case 2 to 10% in case 3 intensifies the sound radiation, but the directivity remains the same as in case 2. Furthermore, the dominant acoustic sources in case 1 are found on the upstream surface of the cylinder while those in case 2 and 3 are located at $3d$ and $2.5d$ from the downstream surface of the cylinder.

REFERENCES

Bagchi, P. and Balachandar, S. (2004) *Response of the Wake of an Isolated Particle to an Isotropic Turbulent Flow* Journal of Fluid Mechanics, 518, 95-123.

Bogey, C. and Bailly, C. (2004) *A Family of Low Dispersive and Low Dissipative Explicit Schemes for Flow and Noise Computation* Journal of Computational Physics, 194, 194-214.

Colonus, T., Lele, S.K. and Moin, P. (1997) *Sound Generation in a Mixing Layer* Journal of Fluid Mechanics, 330, 375-409.

Coutanceau, M. and Bouard, R. (1979) *Experimental Determination of the Main Features of the Viscous Flow in the Wake of a Circular Cylinder in Uniform Translation. Part 1. Steady Flow* Journal of Fluid Mechanics, 79 (2), 231-256.

Dennis, S. C. R. and Chang, G.Z. (1970) *Numerical Solutions for Steady Flow Past a Circular Cylinder at Reynolds Numbers up to 100* Journal of Fluid Mechanics, 42 (3), 471-489.

Gore, R.A. and Crowe, C. T. (1989) *Effect of Particle Size on Modulating Turbulent Intensity* International Journal of Multiphase Flow, 15 (2), 279-285.

Hestroni, G. (1989) *Particle-Turbulence Interaction* International Journal of Multiphase Flow, 15 (5), 735-746.

Hu, F.Q. (2001) *A Stable, Perfectly Matched Layer for Linearized Euler Equations in Unsplit Physical Variables* Journal of Computational Physics, 173, 455-480.

- Iida, A., Mizuno A. and Brown, R.J. (2004) *Identification of Aerodynamic Sound Source in the Wake of a Rotating Circular Cylinder* Proceeding of the 15th Australasian Fluid Mechanics Conference, Sydney.
- Inoue, O. and Hatakeyama, N. (2002) *Sound Generation by a Two-Dimensional Circular Cylinder in a Uniform Flow* Journal of Fluid Mechanics, 471, 285-314.
- Larsson, J. (2002) *Computational Aero Acoustics for Vehicles Applications* Licentiate Degree Thesis, Chalmers University of Technology.
- Mittal, R. (2000) *Response of the Sphere Wake to Freestream Fluctuations* Theoretical and Computational Fluid Dynamics, 13, 397-419.
- Ribner, H.S. (1959) *New Theory of Jet-Noise Generation, Directionality and Spectra* Journal of Acoustical Society of America, 31, 245-246.
- Shen, W.Z., Michelsen, J.A. and Sorensen, J.N. (2004) *A Collocated Grid Finite Volume Method for Aeroacoustic Computations of Low-Speed Flows* Journal of Computational Physics, 196, 348-366.
- Streett, C.L. and Hussaini, M. Y. (1991) *A Numerical Simulation of the Appearance of Chaos in Finite-Length Taylor-Coutte Flow* Applied Numerical Mathematics, 7, 41-71.